INTERNATIONAL JOURNAL OF HYDROGEN ENERGY 48 (2023) 28747–28757

Available online at www.sciencedirect.com

ScienceDirect

journal homepage: www.elsevier.com/locate/he

Novel synthesis of Ti–Fe_2O_3/MIL-53(Fe) via the in situ process for efficient photoelectrochemical water oxidation

Kaikai Ba, Kai Zhang, Zhijun Liang, Yunan Liu, Yanhong Lin, Dejun Wang, Tengfeng Xie, Jun Li***

Institute of Physical Chemistry, College of Chemistry, Jilin University, Changchun 130012, PR China

HIGHLIGHTS

- Ti–Fe_2O_3/MIL-53(Fe) photoelectrode was successfully constructed.
- Ti–Fe_2O_3/MIL-53(Fe) reaches 2.5 mA/cm^2 at 1.23 V vs. RHE, which is 10 times that of bare Ti–Fe_2O_3.
- MIL-53(Fe) greatly improves the water oxidation reaction kinetics of Ti–Fe_2O_3.
- This work provides a new insight into charge transfer in inorganic-organic hybrid systems.

GRAPHICAL ABSTRACT

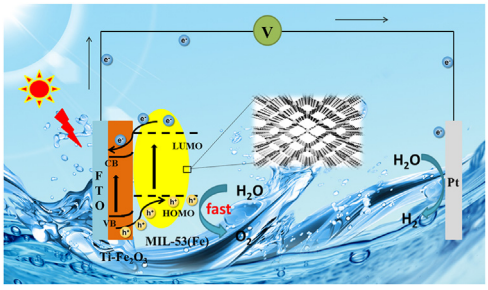

ARTICLE INFO

Article history:
Received 30 January 2023
Received in revised form
29 March 2023
Accepted 8 April 2023
Available online 25 April 2023

Keywords:
Ti–Fe_2O_3 photoanode
Metal-organic frameworks
In situ etching
Cocatalyst
Water oxidation

ABSTRACT

The slow kinetics of water oxidation has become a challenge for photoelectrochemical hydrogen production. Here, a novel organic-inorganic integrated photoanode system was constructed by using MIL-53(Fe) formed during the in-situ etching process as a cocatalyst to modify Ti–Fe_2O_3. The photocurrent density of Ti–Fe_2O_3/MIL-53(Fe) reaches 2.5 mA/cm^2, 10 times that of bare Ti–Fe_2O_3 at 1.23 V vs. RHE, and the water oxidation photocurrent onset potential shifts 105 mV negatively. Ti–Fe_2O_3/MIL-53(Fe) reaches 52% at 390 nm for IPCE. The excellent photoelectrochemical performance is due to iron oxide clusters boost charge separation and transfer, in-situ etching exposes more reactive sites, and the tight connection reduces interfacial resistance, which greatly accelerates the surface kinetics of Ti–Fe_2O_3. The in-depth understanding is provided for in-situ modification of photoanodes by metal organic frameworks in this work.

* *Corresponding author.*
** *Corresponding author.*
E-mail addresses: xietf@jlu.edu.cn (T. Xie), lj98998@jlu.edu.cn (J. Li).
https://doi.org/10.1016/j.ijhydene.2023.04.092

Introduction

Photochemical (PEC) water splitting, as a means of producing hydrogen, is considered as a potential way to solve the current energy problem [1–3]. In the whole reaction, the oxygen evolution semireaction (OER) has become the rate-control step of water splitting because its Gibbs free energy is greater than zero and the reaction rate is relatively slow [4]. Therefore, it is very important to find a photoanode material with high photoelectric conversion efficiency. Among many materials, α-Fe_2O_3 has become one of the most attractive photoanodes, such as narrow band gap (~2.1 eV), low cost, etc [5]. Its surface unfavorable water oxidation kinetics and carriers recombination, however, limit the further application of α-Fe_2O_3.

In view of the above shortcomings, many excellent oxygen evolution catalysts are used to modify Fe_2O_3, such as FeOOH [6], Co-Pi [7], NiFe-LDHs [8], etc. Generally speaking, oxygen evolution catalysts mainly play the role of extracting holes from semiconductors, passivating surface states, increasing active sites and accelerating the kinetics of water oxidation [9,10]. In recent years, metal organic frameworks (MOFs) are increasingly used in oxygen evolution reaction due to their huge specific surface area and controllable metal active centers. In various MOFs, MIL-53(Fe) with simple synthesis method, small band gap and excellent photocatalytic performance, with the molecular formula of $Fe^{III}(OH)\{O_2C-C_6H_4-CO_2\}$, has attracted wide attention [11]. Yang et al. synthesized MIL-53(Fe)/metal phenolic network (Ni, Co and Mn) nanostructures, which exhibited good OER performance. The presence of MIL-53(Fe) enhanced the adsorption capacity of OH^- in the nanostructures [12]. Qiu et al. developed a spindle shaped MIL-53(Fe)–NH_2@$ZnIn_2S_4$ photocatalyst with a Z-scheme heterostructure for photocatalytic oxidation of aromatic alcohols in air under visible light [13]. Bi et al. proved that MIL-53(Fe) can be used as an effective hole transfer cocatalyst, which significantly improved the PEC performance of 2% Mo: $BiVO_4$ photoanode for water oxidation under solar irradiation [14]. Jiang et al. reported a novel composite of Ni_3S_2/MIL-53(Fe) nanosheet arrays, which achieves high conductivity to promote charge transfer, and has rich coordination unsaturated centers to provide a large number of active sites, exhibiting excellent OER performance [15]. The close connection between MOF and semiconductor is necessary for excellent photoanode. Few studies, however, have explored the PEC performance and photogenerated charge behavior of MIL-53(Fe) coating on Fe_2O_3.

In this work, we synthesized closely bound MIL-53(Fe) on Ti–Fe_2O_3 through in situ etching process. As a cocatalyst, MIL-53(Fe) exposes abundant unsaturated Fe sites, greatly speeds up the surface kinetics of Ti–Fe_2O_3, and promotes the separation of charges. Thus, Ti–Fe_2O_3/MIL-53(Fe) exhibits a significantly enhanced photocurrent density and incident photon-to-current conversion efficiency (IPCE). This study opens up an effective way to significantly improve the solar-energy conversion efficiency of Ti–Fe_2O_3 photoanode.

Experimental section

Sample preparation

Synthesis of Ti–Fe_2O_3

Ti–Fe_2O_3 arrays were prepared by simple hydrothermal method [16]. In terms of details, 3 mmol $FeCl_3.6H_2O$ and 20 mmol $NaNO_3$ were dissolved in 20 ml deionized water in turn, and 30 μL titanium tetrachloride ethanol solution with volume ratio of 0.05% is injected into above solution. The solution is then poured in autoclave containing FTO and heated for 10 h at 100 °C. Take out the yellow FeOOH/FTO in the reactor after the reaction, wash it with deionized water, and dry it naturally. Finally, put the yellow film into a muffle furnace and heat it for 2 h at 550 °C, the obtained sample is named Ti–Fe_2O_3.

Synthesis of Ti–Fe_2O_3/MIL-53(Fe)

Ti–Fe_2O_3/MIL-53(Fe) is synthesized by two-step method. First, a three electrode system is used to deposit iron base hydroxide on Ti–Fe_2O_3 by electrodeposition. In the three electrode system, platinum wire is the counter electrode, the electrolyte is 0.05 M $FeSO_4.7H_2O$, the application potential is −0.1 V vs. Ag/AgCl, and deposited for 30 s. After deposition, wash it with deionized water and dry overnight. The obtained photoanode is named Ti–Fe_2O_3/$Fe(OH)_x$.

Second, the obtained Ti–Fe_2O_3/$Fe(OH)_x$ is etched by solvothermal method to obtain Ti–Fe_2O_3/MIL-53(Fe). In detail, 0.08 M terephthalic acid is dissolved in 40 ml DMF and stirred evenly to become transparent. Then transfer the solution to the reactor containing Ti–Fe_2O_3/$Fe(OH)_x$, and put it into the electric blast drying oven for heating for 9 h at 150 °C. Take out the sample after cooling and wash it with DMF and anhydrous ethanol for three times in turn, vacuum drying at 60 °C for 6 h, and the final sample is named Ti–Fe_2O_3/MIL-53(Fe).

Characterization

The crystal phase structure of photoanodes between 5 and 50° was studied by X-ray diffraction (XRD). The morphology of photoanodes was studied by field emission scanning electron microscopy (FE-SEM). The element states of photoanodes were investigated by X-ray photoelectron spectroscopy (XPS), and C1s peak was used for correction. Transmission electron microscopy (TEM) was used to study the specific nanostructures of photoanodes. The optical characteristics of photoanodes were characterized by UV/vis DRS.

Phase locked surface photovoltage spectroscopy (SPV) was used to study the separation and transfer of photogenerated charges. The SPV test was completed between 300 and 800 nm, 24 Hz, including the lock-in amplifier (SB830-DPS), optical chopper (SR540), data processor, 500 W Xe-lamp (CHF-XM-500 W) and monochromator (ZLolix SBP500).

PEC measurements

The electrochemical station (CHI-660 E) equipped with a standard three electrode system is used for the

photoelectrochemical test under AM 1.5 G, 100 mW/cm^2 in 1 M KOH (pH = 13.6), in which Ag/AgCl as the reference electrode and platinum wire as counter electrode, the reaction area is 0.283 square centimeters. The Nyquist plots are conducted in the frequency range of 5×10^{-2}-10^5 Hz and a 20 mV amplitude perturbation under AM 1.5 G illumination at 1.0 V vs. RHE. Mott-Schottky plots were measured using an AC signal (frequency of 1 kHz) in the dark.

Results and discussions

Synthesis and characterization

Scheme 1 is the synthesis process of Ti–Fe_2O_3/MIL-53(Fe). The layered iron hydroxide is first deposited on Ti–Fe_2O_3 by electrodeposition, and then in-situ etched by solvothermal method. The $Fe(OH)_x$ is gradually dissolved by H^+ from terephthalic acid, and exposed Fe^{3+} sites are unsaturated coordinated by ligands to form MIL-53(Fe).

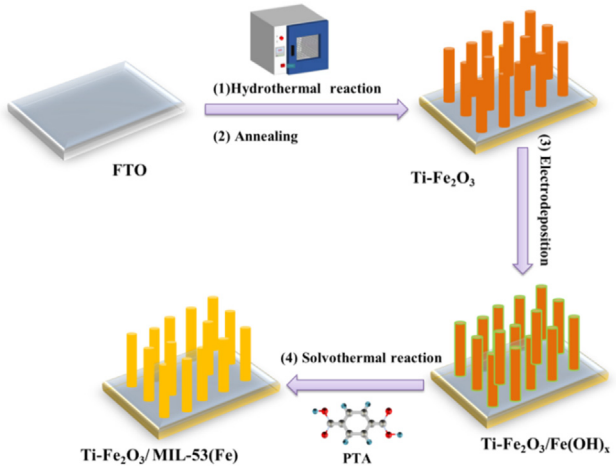

Scheme 1 – The synthesis process of Ti–Fe_2O_3/MIL-53(Fe) photoanode.

From SEM images, it can be seen that Ti–Fe_2O_3 is composed of nanorods arrays with a diameter of about 50 nm in Figs. S1–S2 and Fig. 1a. After potentiostatic electrodeposition, it is found that the nanorod array is covered with layered iron hydroxide (Fig. 1b). Finally, the hydroxide disappears after solvothermal etching (Fig. 1c). The nanostructure morphology of Ti–Fe_2O_3/MIL-53(Fe) was further studied by TEM in Fig. 1d. It was clearly observed that Ti–Fe_2O_3 nanorods were tightly wrapped by an 6 nm amorphous layer (Fig. 1e). The 0.22 nm lattice stripe in the HR-TEM image Fig. 1f corresponds to the (113) plane of α-Fe_2O_3, which proves the successful synthesis of Ti–Fe_2O_3 [17]. In the transmission electron microscope energy spectrum scanning, C, Fe, O, Ti and other elements were found to be uniformly distributed on Ti–Fe_2O_3/MIL-53(Fe) (Fig. 2), which indirectly proved the synthesis of Ti–Fe_2O_3/MIL-53(Fe) photoanode.

In Fig. 3a, the XRD diffraction peaks of all photoanodes at 33.6° and 40.8° correspond to α-Fe_2O_3 (JCPDS, No. 33–0664), while the diffraction peaks at 24.5°, 35.6° and 37.7° are from the FTO glass substrate [18]. When $Fe(OH)_x$ is deposited on Ti–Fe_2O_3, no additional diffraction peaks are found, which was related to its amorphous structure. When $Fe(OH)_x$ is in-situ etched by terephthalic acid and converted to Fe-based MOF, a new diffraction peak (9.1°) appears in Fig. 3b, which is consistent with the MIL-53(Fe) simulated XRD model and the report on MIL-53(Fe) in the literature, directly confirming the successful growth of MIL-53(Fe) on Ti–Fe_2O_3 [19,20]. To further verify the existence of MIL-53(Fe) on Ti–Fe_2O_3, the characteristic functional groups were detected by FT-IR. The absorption peak at 3441 cm^{-1} in Fig. 3c, which can be assigned to the –OH group or H_2O [21]. The characteristic peaks at 1641 and 1386 cm^{-1} are the symmetric vibration of C=O and C–O groups, respectively, and the characteristic peaks at 1544 and 1462 cm^{-1} are confirmed to be the vibration of –COOH

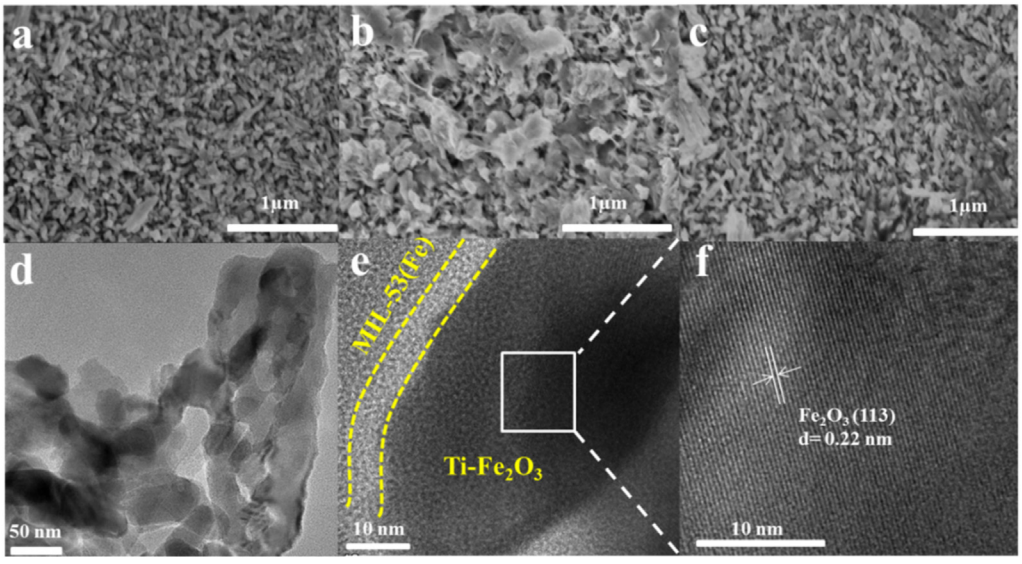

Fig. 1 – SEM images of (a) Ti–Fe_2O_3, (b) Ti–Fe_2O_3/$Fe(OH)_x$, (c) Ti–Fe_2O_3/MIL-53(Fe). (d) TEM image of Ti–Fe_2O_3/MIL-53(Fe). (e) and (f) HR-TEM image of Ti–Fe_2O_3/MIL-53(Fe).

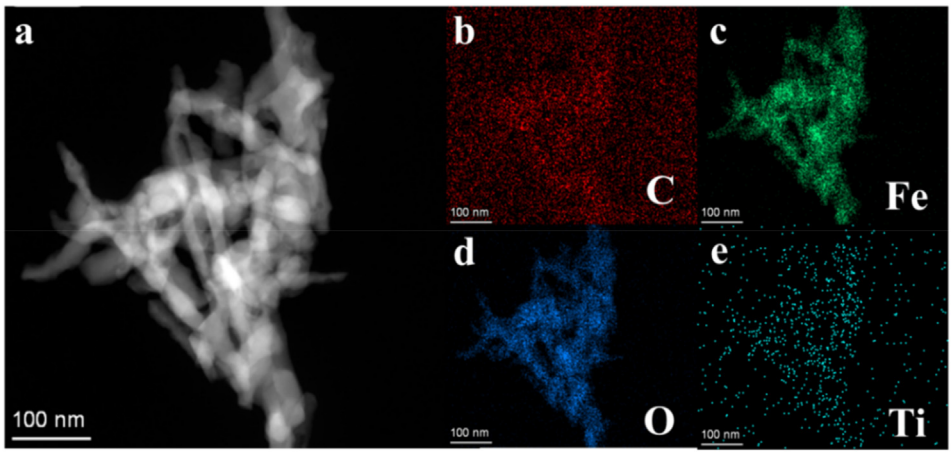

Fig. 2 – EDS elemental mapping of C, Fe, O, Ti of Ti–Fe_2O_3/MIL-53(Fe).

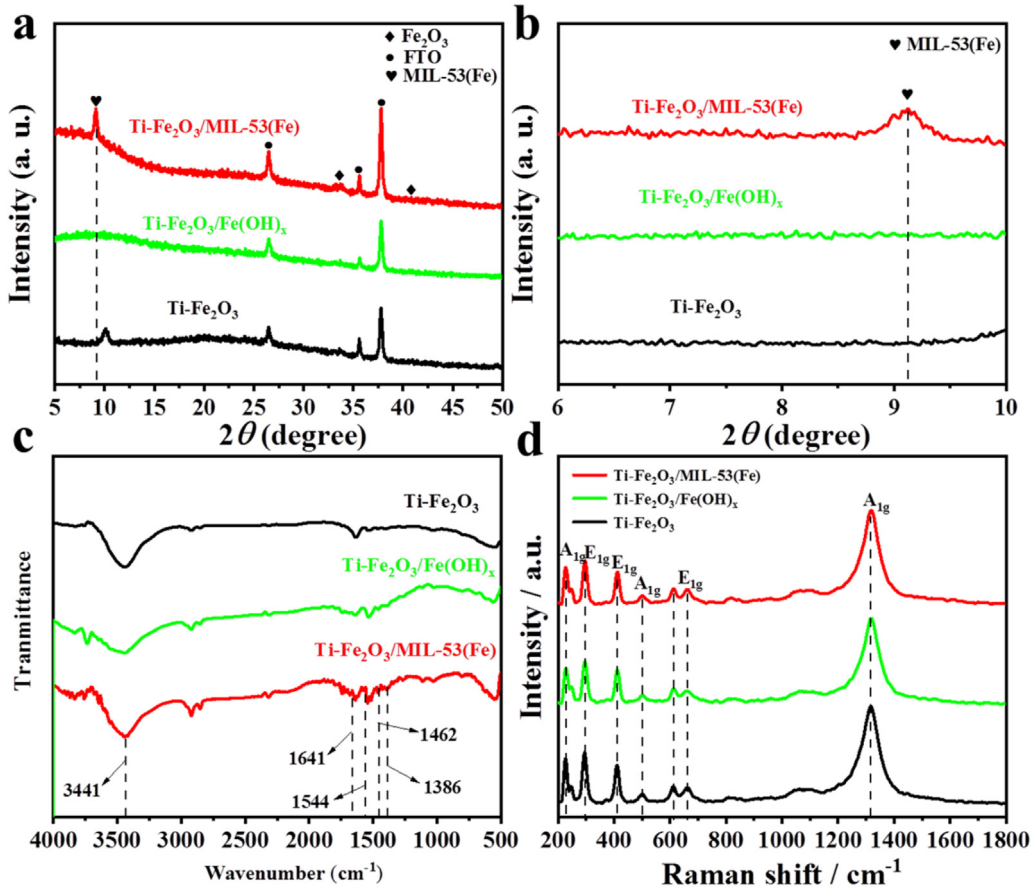

Fig. 3 – (a) XRD patterns, (b) enlarged XRD patterns, (c) FTIR spectra, (d) Raman spectra of Ti–Fe_2O_3, Ti–Fe_2O_3/$Fe(OH)_x$, Ti–Fe_2O_3/MIL-53(Fe).

groups [22]. Combined with XRD results, it is proved that $Fe(OH)_x$ was successfully etched in situ and finally formed MIL-53(Fe) on Ti–Fe_2O_3. The Raman spectrum analyzed the local structure of all photoanodes in Fig. 3d. Ti–Fe_2O_3/MIL-53(Fe) showed a positive shift at the main peak of 1318.4 cm^{-1} compared with Ti–Fe_2O_3, indicating the successful synthesis of MIL-53(Fe) and its influence on the local crystal structure of Ti–Fe_2O_3 [23].

To further study the element composition of Ti–Fe_2O_3/MIL-53(Fe), the chemical information of photoanodes surface was analyzed by XPS. In O 1s (Fig. 4a), the peak at 529.9 eV is related to the metal oxygen bond, and peaks at 532.5 eV and 531.5 eV are related to the carbon oxygen double bond (C═O) and the hydroxyl oxygen adsorbed on the surface (—OH), respectively [24]. Compared with bare Ti–Fe_2O_3, the binding energy of O 1s in Ti–Fe_2O_3/MIL-53(Fe) has a significant positive

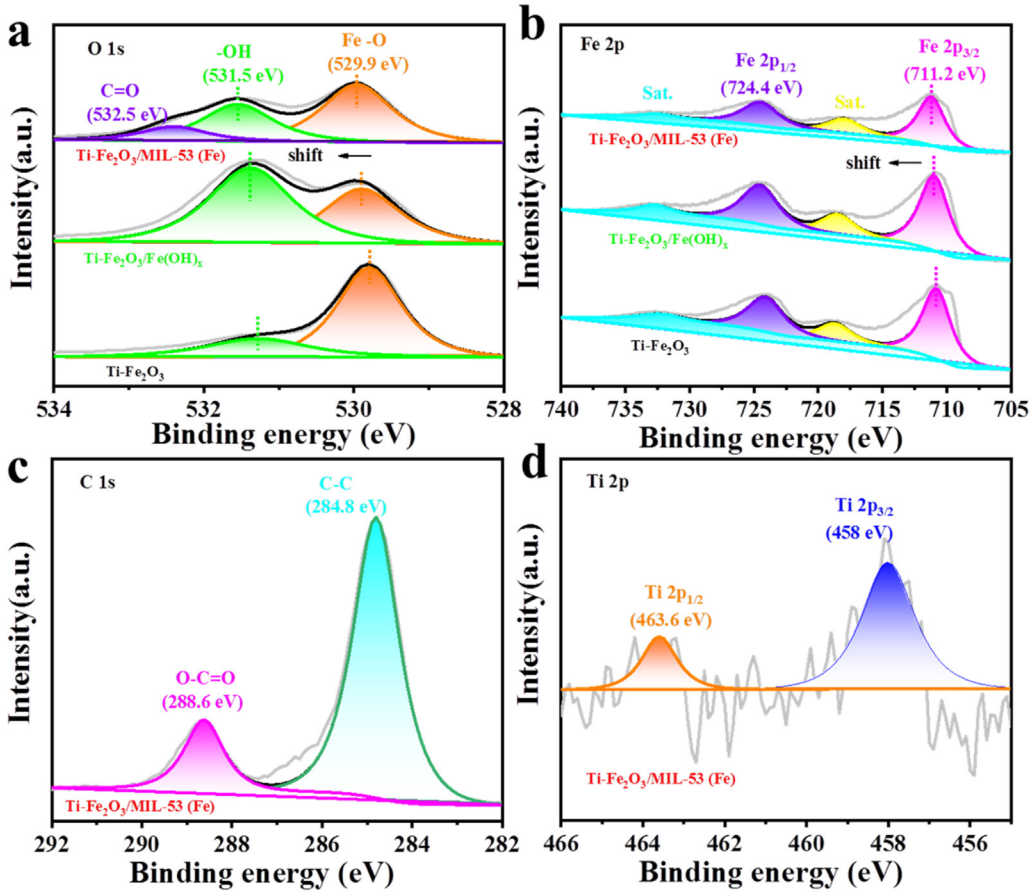

Fig. 4 – XPS spectra (a) O_{1s}, (b) Fe_{2p} of Ti–Fe_2O_3, Ti–Fe_2O_3/Fe(OH)$_x$ and Ti–Fe_2O_3/MIL-53(Fe). (c) C_{1s}, (d) Ti_{2p} of Ti–Fe_2O_3/MIL-53(Fe).

shift, and the binding energy of Fe 2p moves to a higher value (Fig. 4b), manifesting that the electron transfers from MIL-53(Fe) to Ti–Fe_2O_3 [25]. The peaks at 724.4 eV and 711.2 eV correspond to Fe $2p_{1/2}$ and Fe $2p_{3/2}$, respectively [26]. The peaks at 284.8 eV and 288.6 eV in the XPS spectrum of C 1s belong to C=C attributed to phenyl group and C=O attributed to carboxyl group, respectively (Fig. 4c) [27]. The surface of Ti–Fe_2O_3 is covered by MIL-53(Fe) layer, the characteristic peak of Ti^{4+} is relatively weak, appearing at 458 eV and 463.6 eV in Fig. 4d [28]. According to the above XPS results, MIL-53(Fe) layer is successfully covered on Ti–Fe_2O_3 nanorods, and there is electronic coupling on the interface between Ti–Fe_2O_3 and MIL-53(Fe), which is conducive to promoting the transfer of charges.

In Fig. 5a, the absorption edge of Ti–Fe_2O_3 is located at 590 nm, and the band gap calculated is about 2.1 eV (Fig. 5b) [29]. It is worth noting that after MIL-53(Fe) layer is modified, the absorption intensity of Ti–Fe_2O_3/MIL-53(Fe) photoanode increases at 400 nm, which may be due to the transition ($^6A_{1g}$ => $^4A_{1g}$ + ^4E_g(G)) in Fe (III) of MIL-53(Fe) [30,31].

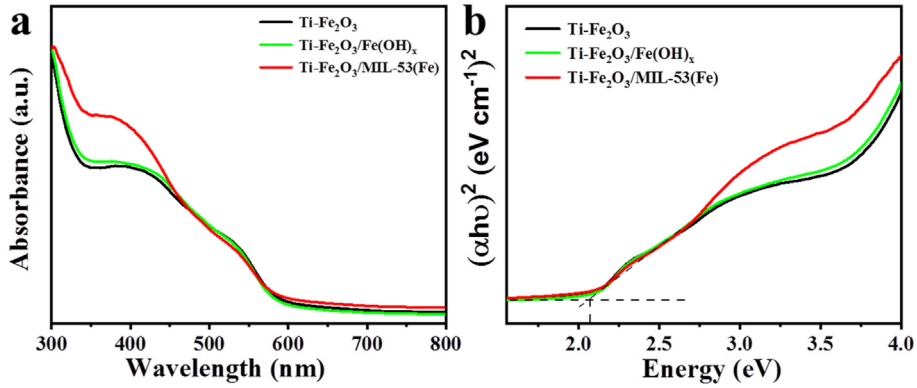

Fig. 5 – (a) UV–vis spectra, (b) Tauc plot of Ti–Fe_2O_3, Ti–Fe_2O_3/Fe(OH)$_x$, Ti–Fe_2O_3/MIL-53(Fe).

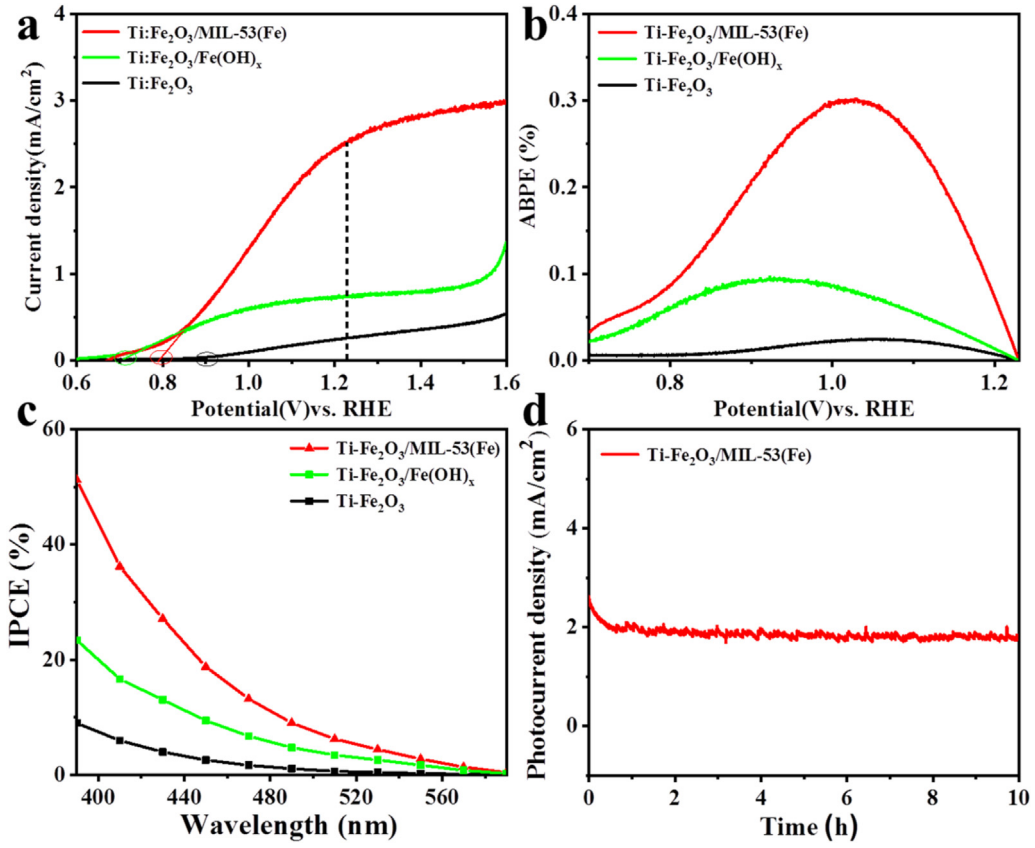

Fig. 6 – (a) Linear voltammetric sweep curves under AM 1.5 G illumination, (b) IPCE values at 1.23 V vs. RHE, (c) ABPE values of Ti–Fe_2O_3, Ti–Fe_2O_3/Fe(OH)$_x$, Ti–Fe_2O_3/MIL-53(Fe). (d) Photostability measurement of Ti–Fe_2O_3/MIL-53(Fe).

PEC properties of Ti–Fe_2O_3/MIL-53(Fe) photoanodes

The photoelectrochemistry performance of Ti–Fe_2O_3/MIL-53(Fe) was measured by linear scanning voltammetry (LSV) in 1 M potassium hydroxide (Fig. 6a). The photocurrent density of Ti–Fe_2O_3/MIL-53(Fe) photoanode reaches 2.5 mA/cm^2, about 10 times that of bare Ti–Fe_2O_3 (0.25 mA/cm^2) at 1.23 V vs. RHE, and the water oxidation photocurrent onset potential shifts 105 mV negatively. In addition, Ti–Fe_2O_3/Fe(OH)$_x$ shows more significant cathodic shift, indicating that Fe(OH)$_x$ has excellent electrocatalytic performance. The optimal deposition time and etching time are 30 s and 9 h (Figs. S3 and S4), respectively. From Table S1, Ti–Fe_2O_3/MIL-53(Fe) shows excellent performance. The maximum ABPE value of Ti–Fe_2O_3/MIL-53(Fe) is 0.29% in Fig. 6b, which is much higher than that of Ti–Fe_2O_3 and Ti–Fe_2O_3/Fe(OH)$_x$. Moreover, the IPCE value of Ti–Fe_2O_3/MIL-53(Fe) at 390 nm is 52%, about 6 times that of Ti–Fe_2O_3, efficiently improving the photoelectric conversion efficiency of Ti–Fe_2O_3 (Fig. 6c), which is due to that the Fe–O clusters in MIL-53(Fe) promote hole electron pair separation under the excitation of light [32]. During the stability test, Ti–Fe_2O_3/MIL-53(Fe) can still maintain 75% of the initial photocurrent density under 10 h of continuous light (Fig. 6d), which shows that Ti–Fe_2O_3/MIL-53(Fe) has good durability.

Separation and transfer of photogenerated charge carriers

To further clarify the effect of MIL-53(Fe) layer on the photogenerated charge behavior of composite photoanode, the charge separation efficiency (η_{sep}) is first measured by adding H_2O_2 as the hole scavenger in KOH [33]. In Fig. 7a, η_{sep} of Ti–Fe_2O_3/MIL-53(Fe) performs better than Ti–Fe_2O_3 and Ti–Fe_2O_3/Fe(OH)$_x$. Specifically, η_{sep} of Ti–Fe_2O_3/MIL-53(Fe) is 29%, which is 1.3 times and 1.2 times of Ti–Fe_2O_3 (21%) and Ti–Fe_2O_3/Fe(OH)$_x$ (22%), respectively. Subsequently, we characterize the separation performance of the generated charge at the interface by open circuit photovoltage when photoanode contacts with the electrolyte in Fig. 7b [34]. The open circuit photovoltage (OCPV) is obtained by the difference value of the photoanode open circuit voltage (V_{oc}) in the light and dark states. V_{oc} in the dark usually reflects the degree of upward band bending when photoanode and electrolyte balance, and the more positive indicates the more obvious upward band bending, which may be related to the passivation of the surface state of Fe_2O_3 to unlock Fermi energy level pinning [35]. The calculated open circuit photovoltage values are 0.15 V (Ti–Fe_2O_3), 0.17 V (Ti–Fe_2O_3/Fe(OH)$_x$) and 0.2 V (Ti–Fe_2O_3/MIL-53(Fe)), respectively, which proves that after the introduction of MIL-53(Fe) and Fe(OH)$_x$, due to the increase of the upward band bending, a stronger interfacial electric field is formed

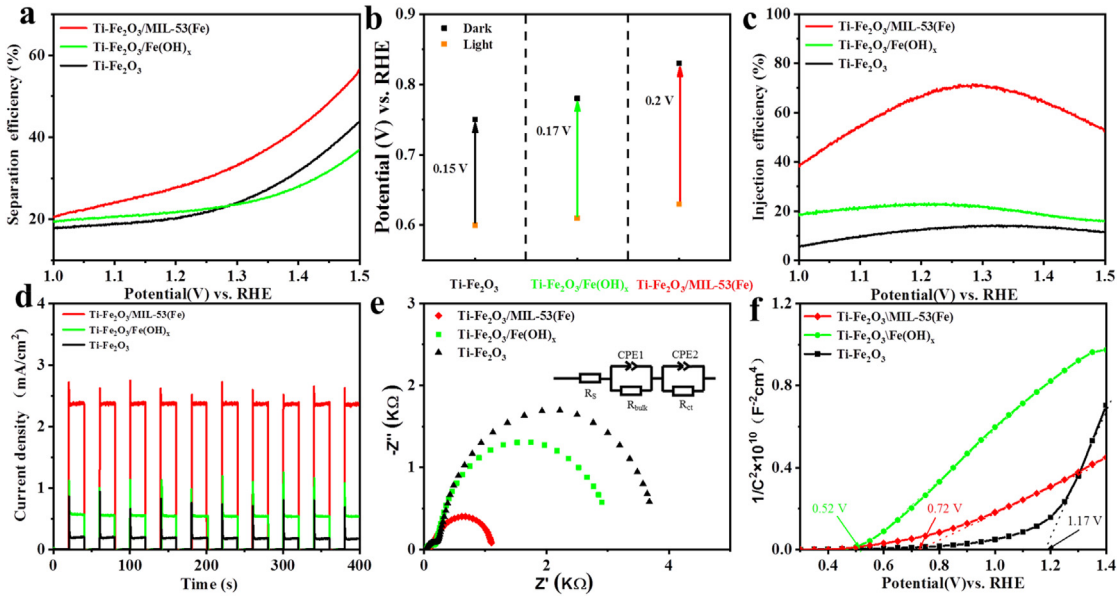

Fig. 7 – (a) η_{sep}, (b) OCPV in 1 M KOH electrolyte, (c) η_{inj}, (d) J-t curves under chopped light illumination, (e) Nyquist plots under AM 1.5 G illumination, (f) Mott-Schottky plots in dark of Ti–Fe_2O_3/MIL-53(Fe), Ti–Fe_2O_3/Fe(OH)$_x$ and Ti–Fe_2O_3 photoanodes.

Table 1 – EIS fitting results of Ti–Fe_2O_3/MIL-53(Fe), Ti–Fe_2O_3/Fe(OH)$_x$ and Ti–Fe_2O_3 photoanodes.

Photoanode	Rs(Ω)	Rbulk (Ω)	CPE1(F.cm^{-2})	R_{ct} (Ω)	CPE2(F.cm^{-2})
Ti–Fe_2O_3	32.54	207.3	6.706×10^{-6}	3695	1.475×10^{-4}
Ti–Fe_2O_3/Fe(OH)$_x$	40.13	154.8	6.929×10^{-6}	2957	2.291×10^{-4}
Ti–Fe_2O_3/MIL-53(Fe)	61.01	63.23	1.321×10^{-5}	1029	2.442×10^{-4}

between the solid-liquid interface, resulting in the separation of carriers [36].

To explore the influence of cocatalyst MIL-53(Fe) on Ti–Fe_2O_3 water oxidation kinetics, we obtained the charge injection efficiency (η_{inj}) by using the ratio of hydrogen peroxide hole scavenger and hole free scavenger's photocurrent density value [37]. The linear voltammetric scan curves obtained in an electrolyte containing a hole scavenger (H_2O_2) are shown in Figs. S5–S7. The η_{inj} of bare Ti–Fe_2O_3 photoanode is 14% at 1.23 V vs. RHE (Fig. 7c), when MIL-53(Fe) is added, the η_{inj} reaches 69%, which may be the good dispersion of metal oxygen clusters that makes the carriers generated by photons easier to contact the reactants, significantly promotes the kinetics of water oxidation. At the same time, the J-t test under chopped light (Fig. 7d) reveals photoanodes have good response to light. The transient anodic current peak of Ti–Fe_2O_3/MIL-53(Fe) is significantly smaller than that of Ti–Fe_2O_3, indicating that the charge transfer at the photoanode/electrolyte interface is more smooth and the charge surface recombination is suppressed.

The charge transfer characteristics of photoanodes were further characterized by the Nyquist plots at 1.0 V vs. RHE under AM 1.5 G illumination, as shown in Fig. 7e. The arc in the low frequency region is related to the charge transfer resistance at the solid-liquid interface, and the smaller the arc, the smaller the resistance [38]. Obviously, the arc of Ti–Fe_2O_3/MIL-53(Fe) is smaller than that of Ti–Fe_2O_3/Fe(OH)$_x$, and much smaller than that of Ti–Fe_2O_3, indicating MIL-53(Fe) significantly accelerates holes injection to electrolyte. The fitting value obtained by using the typical equivalent circuit model is shown in Table 1, where R_{bulk} is related to the charge-transfer resistance in bulk photoanodes and R_{ct} corresponds to transport resistance at the interface of photoanode and electrolyte [39]. The Ti–Fe_2O_3/MIL-53(Fe) displays the smallest R_{bulk} among all photoanodes, indicating the lowest charge-transport resistance and the highest charge-transfer efficiency in the bulk, as shown in Table 1 and Fig. S8. The R_{ct} value of Ti–Fe_2O_3/MIL-53(Fe) photoanode is 151.6 Ω, which is less than that of Ti–Fe_2O_3/Fe(OH)$_x$ (243.2.2 Ω) and bare Ti–Fe_2O_3 (776.1 Ω) photoanode, resulting in more favorable charge transfer at solid-liquid interface. This result is consistent with the above PEC measurement, η_{inj} and η_{sep} observations. Mott Schottky diagrams of all photoanodes are recorded in the dark (Fig. 7f). All curves have a positive slope, indicating that these photoanodes have the property of n-type semiconductor [40]. Compared with bare Ti–Fe_2O_3 photoanode, the flat band potential (E_{fb}) of Ti–Fe_2O_3/MIL-53(Fe) shows a negative shift, indicating that the bending of the band edge increases, thus effectively promoting charges separation [41]. We can calculate the donor concentration (N_d) by the M – S equation. Interestingly, the N_d of Ti–Fe_2O_3/MIL-53(Fe) is 4.8 times that of bare Ti–Fe_2O_3, indicating that MIL-53(Fe) can increase the conductivity of Ti–Fe_2O_3, as shown in Table S2.

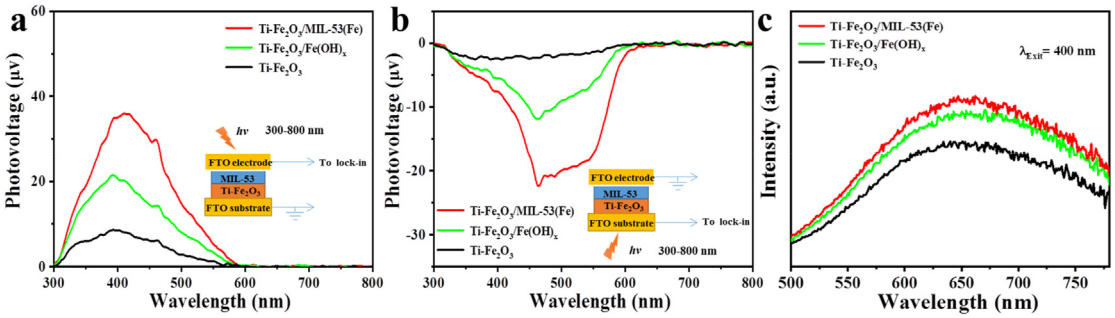

Fig. 8 – (a) SPV signals when illuminating from MIL-53(Fe) side, (b) SPV signals when illuminating from Ti–Fe_2O_3 side, (c) PL spectras of Ti–Fe_2O_3/MIL-53(Fe), Ti–Fe_2O_3/$Fe(OH)_x$ and Ti–Fe_2O_3 photoanodes.

In order to deeply understand the charges behavior after the composite photoanode was successfully constructed, we conducted a steady-state surface photovoltage spectroscopy (SPV) test. According to previous reports, positive signals represent the migration and accumulation of holes to the sample surface, while negative signal indicates electron accumulation to the sample surface, where the response intensity is proportional to the charge separation efficiency [42,43]. In Fig. 8a, the SPV spectrum (MIL-53(Fe) side lighting) of Ti–Fe_2O_3/MIL-53(Fe) photoanode shows significantly stronger positive signal than that of bare Ti–Fe_2O_3, indicating that after Ti–Fe_2O_3 is excited, holes on the valence band under the effect of the interface electric field migrate and accumulate to the HOMO level of MOFs [44]. Then, we change the illumination mode to deeply explore the migration direction of interface charges. In short, the illumination direction is conducted from the Ti–Fe_2O_3 side, and the measured photovoltage signal is the Ti–Fe_2O_3 side. In Fig. 8b, the SPV response (Ti–Fe_2O_3 side lighting) of Ti–Fe_2O_3/MIL-53(Fe) shows a more negative signal in the response range. That is because more electrons on the LUMO energy level of MOFs are transferred to the conduction band of Ti–Fe_2O_3 on the illumination side, as shown in XPS analysis, thus showing a more negative signal. In addition, compared with the bare Ti–Fe_2O_3, the PL intensity of the composite photoanode is further enhanced (Fig. 8c), indicating that the surface states are passivated after covering the Ti–Fe_2O_3 surface with MIL-53(Fe), and the non radiative recombination of charges is highly inhibited, which enhances charge transfer and separation [45].

In addition, electrochemical double-layer capacitance (C_{dl}) can evaluate the number of catalytic active sites [46]. Fig. 9a shows that the C_{dl} of Ti–Fe_2O_3/MIL-53(Fe) is 27.9 mF cm^{-2},

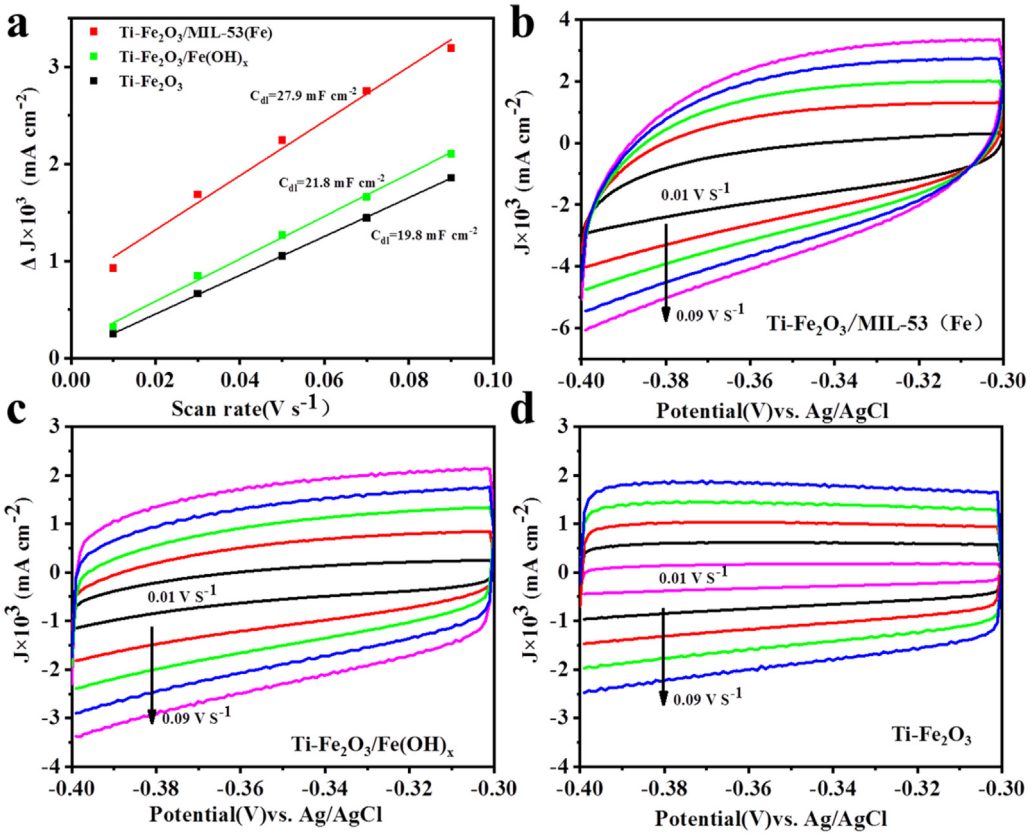

Fig. 9 – (a) Linear fitting of current difference and scanning rate. (b), (c) and (d) CV curves of all photoanodes.

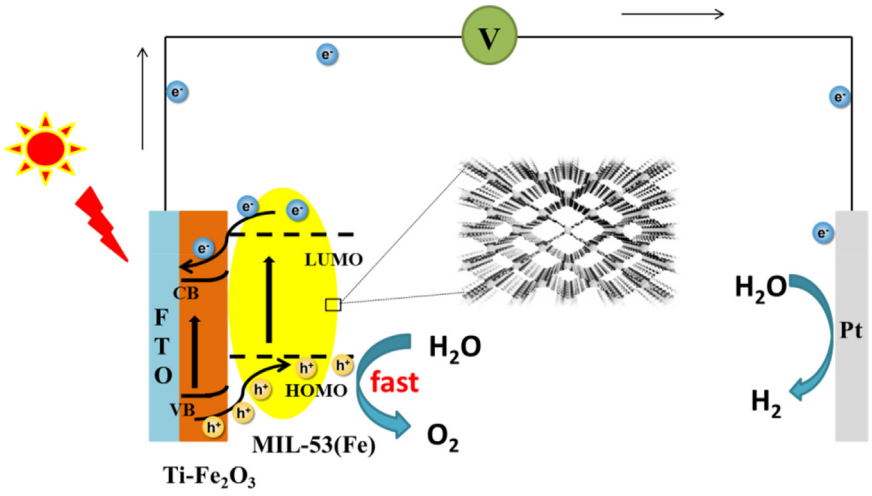

Scheme 2 – Schematic band diagram of Ti–Fe_2O_3/MIL-53(Fe).

significantly higher than that of Ti–Fe_2O_3/$Fe(OH)_x$ (21.8 mF cm^{-2}) and Ti–Fe_2O_3 (19.8 mF cm^{-2}), indicating that the etched Ti–Fe_2O_3/MIL-53(Fe) has more OER active sites (Fig. 9b–d), which is crucial to accelerate the kinetics of water oxidation [47].

In addition, we further evaluated the morphology/composition of Ti–Fe_2O_3/MIL-53(Fe) after 10 h testing to explore the stability of MOF. As shown in Figs. S9a and S9b, Ti–Fe_2O_3/MIL-53(Fe) nanorod is slightly rough, but the overall morphology has not changed much. After the stability test, the symmetrical vibrations of the C=O and C–O groups can still be clearly observed through FTIR characterization of Ti–Fe_2O_3/MIL-53(Fe) in Fig. S10 [21], and a characteristic peak of the carbon oxygen double bond was observed at 532.5 eV in O 1s (Fig. S11a) [23], while the characteristic peak at 288.6 eV in C 1s corresponds to O–C=O (Fig. S11b) [26]. The above results indicate that Ti–Fe_2O_3/MIL-53(Fe) has good stability.

On the basis of above discussion, combined with the results of XPS and steady-state photovoltage, we further propose the charge transfer mechanism on Ti–Fe_2O_3/MIL-53(Fe) during water oxidation in Scheme 2. Both Ti–Fe_2O_3 and MIL-53(Fe) can be excited to generate electron-hole pairs under illumination, electrons will transfer from the LUMO level of MIL-53(Fe) to the conduction band of Ti–Fe_2O_3. Meanwhile, holes migrate from the valence band of Ti–Fe_2O_3 to the HOMO level of MIL-53(Fe) and accumulate, thus effectively separating the hole-electron pairs in Ti–Fe_2O_3/MIL-53(Fe), further improving the PEC performance of water oxidation. In addition, the ultrathin MIL-53(Fe) layer formed on the Ti–Fe_2O_3 surface by in-situ etching not only exposes abundant Fe(III) active sites, but also can consume the captured photogenerated holes faster, greatly accelerating the surface reaction kinetics. Therefore, Ti–Fe_2O_3/MIL-53(Fe) system is important to significantly improve the catalytic activity of PEC water oxidation.

Conclusions

In summary, we successfully synthesized Ti–Fe_2O_3/MIL-53(Fe) photoanode by electrochemical deposition and solvothermal reaction. The photocurrent density of Ti–Fe_2O_3/MIL-53(Fe) reaches 2.5 mA/cm^2, 10 times that of bare Ti–Fe_2O_3 at 1.23 V vs. RHE, and the water oxidation photocurrent onset potential shifts 105 mV negatively. Furthermore, enhanced η_{sep} and η_{inj} as well as excellent stability are observed. The outstanding catalytic activity is due to the following characteristics: (I) solvothermal in-situ etching can provide a good connection between Ti–Fe_2O_3 photoanode and MIL-53(Fe) coating; (II) the iron oxide clusters in MIL-53(Fe) can effectively promote charge transfer and inhibit surface charge recombination. In addition, MIL-53(Fe) formed by in-situ etching can provide more active sites, thereby significantly improving the catalytic activity of PEC water oxidation. The in-depth understanding is provided for charge transfer in inorganic-organic hybrid systems in this work.

Declaration of competing interest

The authors declare that they have no known competing financial interests or personal relationships that could have appeared to influence the work reported in this paper.

Acknowledgements

This work was financially supported by the National Natural Science Foundation of China (Grant Nos. 22172057, 21773086, 21872063).

Appendix A. Supplementary data

Supplementary data to this article can be found online at https://doi.org/10.1016/j.ijhydene.2023.04.092.

REFERENCES

[1] Fujishima A, Honda K. Electrochemical photolysis of water at a semiconductor electrode. Nature 1972;238(5358):37–8.

[2] Cui W, Bai H, Shang J, Wang F, Xu D, Ding J, Fan W, Shi W. Organic-inorganic hybrid-photoanode built from NiFe-MOF and TiO_2 for efficient PEC water splitting. Electrochim Acta 2020;349:136383.
[3] Masoumi Z, Tayebi M, Kolaei M, Tayyebi A, Ryu H, Jang JI, Lee B-K. Simultaneous enhancement of charge separation and hole transportation in a W: alpha-Fe_2O_3/MoS_2 photoanode: a collaborative approach of MoS_2 as a heterojunction and W as a metal dopant. ACS Appl Mater Interfaces 2021;13(33):39215–29.
[4] Gao Y, Li X, Hu J, Fan W, Wang F, Xu D, Ding J, Bai H, Shi W. Ag-Pi/$BiVO_4$ heterojunction with efficient interface carrier transport for photoelectrochemical water splitting. J Colloid Interface Sci 2020;579:619–27.
[5] Yu L, Fan W, He N, Liu Y, Han X, Qin F, Ding J, Zhu G, Bai H, Shi W. Effect of unsaturated coordination on photoelectrochemical properties of Ni-MOF/TiO_2 photoanode for water splitting. Int J Hydrogen Energy 2021;46:17741–50.
[6] Deng J, Zhang Q, Feng K, Lan H, Zhong J, Chaker M, Ma D. Efficient photoelectrochemical water oxidation on hematite with fluorine-doped FeOOH and FeNiOOH as dual cocatalysts. ChemSusChem 2018;11:3783–9.
[7] Bu Q, Li S, Zhang K, Lin Y, Wang D, Zou X, Xie T. Hole transfer channel of ferrihydrite designed between Ti-Fe_2O_3 and CoPi as an efficient and durable photoanode. ACS Sustainable Chem Eng 2019;7:10971–8.
[8] Bu Q, Zhao Q, Sun G, Liu Q, Xie T. Boosting the photogenerated hole separation and injection of Ti-Fe_2O_3 by co-modifying carbon quantum dots and NiFe layered double hydroxide, J. Alloy. Compd 2022;908:164643.
[9] Liu Y, Xia M, Yao L, Mensi M, Ren D, Gratzel M, Sivula K, Guijarro N. Spectroelectrochemical and chemical evidence of surface passivation at zinc ferrite ($ZnFe_2O_4$) photoanodes for solar water oxidation. Adv Funct Mater 2021;31:2010081.
[10] Pang Y, Zang W, Kou Z, Zhang L, Xu G, Lv J, Gao X, Pan Z, Wang J, Wu Y. Assembling of Bi atoms on TiO_2 nanorods boosts photoelectrochemical water splitting of semiconductors. Nanoscale 2020;12:4302–8.
[11] Liang R, Shen L, Jing F, Qin N, Wu L. Preparation of MIL-53(Fe)-Reduced graphene oxide nanocomposites by a simple self-assembly strategy for increasing interfacial contact: efficient visible-light photocatalysts. ACS Appl Mater Interfaces 2015;7:9507–15.
[12] Ji K, Yue Y, Yang P. Interface effect in MIL-53(Fe)/metal-phenolic network (Ni, Co, and Mn) nanoarchitectures for efficient oxygen evolution reaction. Appl Surf Sci 2023;608:155184.
[13] Zhang L, Qiu J, Xia G, Dai D, Zhong X, Yao J. Constructing a Z-scheme Fe-MOF-based heterostructure for visible-light-driven oxidation of aromatic alcohol in ambient air. J Hazard Mater 2023;138:214–20.
[14] Zhang B, Dong G, Wang L, Zhang Y, Ding Y, Bi Y. Efficient hydrogen production from MIL-53(Fe) catalyst-modified Mo:$BiVO_4$ photoelectrodes. Catal Sci Technol 2017;7:4971–6.
[15] Wu F, Guo X, Wang Q, Lu S, Wang J, Hu Y, Hao G, Li Q, Yang M, Jiang W. A hybrid of MIL-53(Fe) and conductive sulfide as a synergistic electrocatalyst for the oxygen evolution reaction. J Mater Chem 2020;8:14574.
[16] Fu Z, Jiang T, Zhang L, Liu B, Wang D, Wang L, Xie T. Surface treatment with Al^{3+} on a Ti-doped alpha-Fe_2O_3 nanorod array photoanode for efficient photoelectrochemical water splitting. J Mater Chem 2014;2(33):13705–12.
[17] Bu Q, Li S, Wu Q, Bi L, Lin Y, Wang D, Zou X, Xie T. Ferrihydrite-modified Ti-Fe_2O_3 as an effective photoanode: the role of interface interactions in enhancing the photocatalytic activity of water oxidation. ChemSusChem 2018;11:3486–94.
[18] Zhang B, Dong G, Wang L, Zhang Y, Ding Y, Bi Y. Efficient hydrogen production from MIL-53(Fe) catalyst-modified Mo:$BiVO_4$ photoelectrodes. Catal Sci Technol 2017;7:4971–6.
[19] He S, Li Tengfei, Zhang L, Zhang X, Ziwen Liu, Zhang Y, Wang J, Jia H, Wang T, Zhu L. Highly effective photocatalytic decomplexation of Cu-EDTA by MIL-53(Fe): highlight the important roles of Fe. Chem Eng J 2021;424:130515.
[20] Yu J, Xiong W, Li X, Yang Z, Cao J, Jia M, Xu R, Zhang Y. Functionalized MIL-53(Fe) as efficient adsorbents for removal of tetracycline antibiotics from aqueous solution. Microporous Mesoporous Mater 2019;290:109642.
[21] Li Y, Wu Q, Bu Q, Zhang K, Lin Y, Wang D, Zou X, Xie T. An effective CdS/Ti-Fe_2O_3 heterojunction photoanode: analyzing Z-scheme charge-transfer mechanism for enhanced photoelectrochemical water-oxidation activity. Chin J Catal 2021;42:762–71.
[22] Xie M, Ma Y, Lin D, Xu C, Xie F, Zeng W. Bimetal-organic framework MIL-53(Co-Fe): efficiency and robust electrocatalyst for the oxygen evolution reaction. Nanoscale 2020;12:67–71.
[23] Liu G, Li Y, Xiao Y, Jia D, Li C, Zheng J, Liu X. Nanoporous Fe-doped $BiVO_4$ modified with MIL-53(Fe) for enhanced photoelectrochemical stability and water splitting perfromances. Catal Lett 2019;149:870–5.
[24] Wang Z, Li H, Yi S, You M, Jing H, Yue X, Zhang Z, Chen D. In-situ coating of multifunctional FeCo-bimetal organic framework nanolayers on hematite photoanode for superior oxygen evolution. Appl Catal B Environ 2021;297:120406.
[25] Cui W, Bai H, Qu K, Wang F, Guan P, Xu D, Fan W, Shi W. In situ decorating coordinatively unsaturated Fe sites for boosting water oxidation performance of TiO_2 photoanode. Energy Technol 2019;7:1801128.
[26] Kormanyos A, Kecsenovity E, Honarfar A, Pullerits T, Janaky C. Hybrid FeNiOOH/alpha-Fe_2O_3/graphene photoelectrodes with advanced water oxidation performance. Adv Funct Mater 2020;30(31):2002124.
[27] Liu C, Luo H, Xu Yu, Zhang Z, Liang Q, Wang W, Chen Z. Synergistic cocatalytic effect of ultra-thin metal-organic framework and Mo-dopant for efficient photoelectrochemical water oxidation on $BiVO_4$ photoanode. Chem Eng J 2020;384:123333.
[28] Cui W, Bai H, Shang J, Wang F, Xu D, Ding J, Fan W, Shi W. Organic-inorganic hybrid-photoanode built from NiFe-MOF and TiO_2 for efficient PEC water splitting. Electrochim Acta 2020;349:136383.
[29] Bu Q, Li S, Wu Q, Bi L, Lin Y, Wang D, Zou X, Xie T. Ferrihydrite-modified Ti–Fe_2O_3 as an effective photoanode: the role of interface interactions in enhancing the photocatalytic activity of water oxidation. ChemSusChem 2018;11:3486–94.
[30] Dong Y, Liao J, Kong Z, Xu Y, Chen Z, Chen H, Kuang D, Fenske D, Su C. Conformal coating of ultrathin metal-organic framework on semiconductor electrode for boosted photoelectrochemical water oxidation. Appl Catal B Environ 2018;237:9–17.
[31] Dang K, Wang T, Li C, Zhang J, Liu S, Gong J. Improved oxygen evolution kinetics and surface states passivation of Ni-Bi Co-catalyst for a hematite photoanode. Engineering 2017;3:285–9.
[32] Li H, Wang Z, Jing H, Yi S, Zhang S, Yue X, Zhang Z, Lu H, Chen D. Synergetic integration of passivation layer and oxygen vacancy on hematite nanoarrays for boosted photoelectrochemical water oxidation. Appl Catal B Environ 2021;284:119760.
[33] Li Y, Wu Q, Chen Y, Zhang R, Li C, Zhang K, Li M, Lin Y, Wang D, Zou X, Xie T. Interface engineering Z-scheme Ti-Fe_2O_3/In_2O_3 photoanode for highly efficient

photoelectrochemical water splitting. Appl Catal B Environ 2021;290:120058.
[34] Berardi S, Cristino V, Canton M, Boaretto R, Argazzi R, Benazzi E, Ganzer L, Varillas RB, Cerullo G, Syrgiannis Z, Rigodanza F, Prato M, Bignozzi CA, Caramori S. Perylene diimide aggregates on Sb-doped SnO_2: charge transfer dynamics relevant to solar fuel generation. J Phys Chem C 2017;121(33):17737–45.
[35] Dong Y, Liao J, Kong Z, Xu Y, Chen Z, Chen H, Kuang D, Fenske D, Su C. Conformal coating of ultrathin metal-organic framework on semiconductor electrode for boosted photoelectrochemical water oxidation. Appl Catal B Environ 2018;237:9–17.
[36] Zheng R, Zhang M, Sun X, Chen R, Sun X. Perylene-3,4,9,10-tetracarboxylic acid accelerated light-driven water oxidation on ultrathin indium oxide porous sheets. Appl Catal B Environ 2019;254:667–76.
[37] Xing C, Yu G, Chen T, Liu S, Sun Q, Liu Q, Hu Y, Liu H, Li X. Perylenetetracarboxylic diimide covalently bonded with mesoporous g-C_3N_4 to construct direct Z-scheme heterojunctions for efficient photocatalytic oxidative coupling of amines. Appl Catal B Environ 2021;298:120534.
[38] Li S, Zhao Q, Meng D, Wang D, Xie T. Fabrication of metallic charge transfer channel between photoanode Ti/Fe_2O_3 and cocatalyst CoO_x: an effective strategy for promoting photoelectrochemical water oxidation. J Mater Chem 2016;4(42):16661–9.
[39] Ba K, Li Y, Zhang R, Zhang K, Liang Z, Liu Y, Lin Y, Wang D, Xie T. Surface selective passivation and $Fe_xNi_{1-x}OOH$ co-modified Fe_2O_3 photoanode toward high-performance water oxidation. Int J Hydrogen Energy 2023;48:3511–9.
[40] Li Y, Wu Q, Bu Q, Zhang K, Lin Y, Wang D, Zou X, Xie T. An effective CdS/Ti-Fe_2O_3 heterojunction photoanode: analyzing Z-scheme charge-transfer mechanism for enhanced photoelectrochemical water-oxidation activity. Chin J Catal 2021;42:762–71.
[41] Li F, Li J, Zhang J, Gao L, Long X, Hu Y, Li S, Jin J, Ma J. NiO nanoparticles anchored on phosphorus-doped-Fe_2O_3 nanoarrays: an efficient hole extraction p-n heterojunction photoanode for water oxidation. ChemSusChem 2018;11(13):2156–64.
[42] Bu Q, Li S, Wu Q, Bi L, Lin Y, Wang D, Zou X, Xie T. Ferrihydrite-modified Ti-Fe_2O_3 as an effective photoanode: the role of interface interactions in enhancing the photocatalytic activity of water oxidation. ChemSusChem 2018;11(19):3486–94.
[43] Li L, Zhang R, Lin Y, Wang D, Xie T. Plasmon-enhanced bulk charge separation via morphological and interfacial engineering in Au@carbon dots@CdS hybrid. Chem Eng J 2023;453:139970.
[44] Li Y, Chen Y, Wu Q, Zhang R, Li M, Lin Y, Wang D, Xie T. Revealing long-lived electron-hole migration in core-shell α/γ-Fe_2O_3/FCP for efficient photoelectrochemical water oxidation. Catal Sci Technol 2022;12:250–8.
[45] Bu Q, Li S, Wu Q, Lin Y, Wang D, Zou X, Xie T. In situ synthesis of FeP-decorated Ti-Fe_2O_3: an effective strategy to improve the interfacial charge transfer in the photoelectrochemical water oxidation reaction. Catal Sci Technol 2019;9:5812–8.
[46] She H, Yue P, Ma X, Huang J, Wang L, Wang Q. Fabrication of $BiVO_4$ photoanode cocatalyzed with NiCo-layered double hydroxide for enhanced photoactivity of water oxidation. Appl Catal B Environ 2020;263:118280.
[47] Bai H, Wang F, You Z, Sun D, Cui J, Fan W. Fabrication of Zn-MOF decorated $BiVO_4$ photoanode for water splitting. Colloids Surf. a-Physicochem. Eng. Asp. 2022;640:128412.